# PROJECTED UV-RESIN CURING FOR SELF-SUPPORTED 3D PRINTING

A Thesis

by

YASUSHI MIZUNO

Submitted to the Office of Graduate and Professional Studies of
Texas A&M University
in partial fulfillment of the requirements for the degree of

MASTER OF SCIENCE

Chair of Committee, Bruce L. Tai
Committee Members, Darren Hartl
M. Cynthia Hipwell
Head of Department, Andreas Polycarpou

December 2018

Major Subject: Mechanical Engineering

# ABSTRACT

This research introduces a new class of additive manufacturing technique for support-free printing. This process uses an array of ultra-violet (UV) laser diodes to immediately cure the jetted photopolymer at the laser intersection; thus, achieving rapid solidification. A prototype system using 405 nm laser array with a jetting device consisting of a piezoelectric pump and a solenoid pin was designed and built. A control scheme for the constructed prototype using traditional machine language was established. Photopolymers used for the experiments were characterized by identifying two dominant properties, penetration depth and critical exposure, by Jacob's working curve method, called windowpane test based on Beer-Lambert's law of exposure. To find a proper range of the printing speed and flowrate, a process model for the proposed printing technique was created by adapting Jacob's model as well as defining the geometry feature deposition model. Using a printing speed of 1 mm/s for a flow rate of 0.5 $mm^3/s$, it was confirmed to create the structure having up to 90-degree overhanging, and a 60-degree overhanging structure can be repeatedly printed with commercially available photopolymers. The study also reveals and discusses the challenges associated with fluid behaviors in such a dynamic condition.

# CONTRIBUTORS AND FUNDING SOURCES

## Contributors

This work was supported by a thesis committee consisting of professors Bruce Tai and Cynthia Hipwell of the Department of Mechanical Engineering, as well as Professor Darren Hartl of the Department of Aerospace Engineering.

The wavelength spectrum data collected for Chapters 2 and 3 were provided by Professor Jamie Grunlan's group. Some sample preparations and measurements for windowpane tests were conducted by Matthew McMahan and Natalie Pardivala, students of mechanical engineering. All other work conducted for the thesis was completed by the student independently.

## Funding Sources

Graduate study was supported by research and teaching assistantship from Texas A&M University. This material is based on work supported by the TEES startup funds.

# NOMENCLATURE

| | |
|---|---|
| 3D | Three-Dimensional |
| AM | Additive Manufacturing |
| CAD | Computer-Aided Design |
| CNC | Computerized Numerical Control |
| cP | Centipoise |
| DLP | Digital Light Processing |
| DOF | Degree of Freedom |
| Hz | Hertz |
| MOSFET | Metal-Oxide-Semiconductor Field-Effect Transistor |
| FDM | Fused Deposition Modeling |
| PID | Proportional-Integral-Derivative controller |
| SLA | Stereolithography |
| SLS | Selective Laser Sintering |
| Tg | Grass transition temperature |
| UV | Ultra-Violet |

TABLE OF CONTENTS

LIST OF FIGURES

Page

LIST OF TABLES

Page

# 1. INTRODUCTION

## 1.1 Support structure in additive manufacturing

Additive manufacturing (AM) technology, known as 3D printing, has shown its potentials to offer a new class of manufacturing with flexible and cost-effective nature. Major AM techniques include Fused Deposition Modeling (FDM), Stereolithography (SLA), Selective Laser Sintering (SLS), and material jetting (PolyJet). These techniques heavily rely on the use of soluble support materials or breakable support structures to create complex three-dimensional (3D) geometries having overhanging structures. For conventional polymeric AM methods based on layer-by-layer process, support structure is necessary for virtually all functional components having overhanging structures. Overhanging structures in AM process can be defined as a part of structure that projected over the structure created by the previous layers. The angle between the projected area and the vertical line is called overhanging angle or unsupported angle. In slicing processes, generating toolpaths of machine from a surface mesh model, the overhanging angle is used as a threshold angle if support structures are needed to apply, as shown in Figure 1 [1]. For example, 45 [2], 45 [3], 0, and 71 degrees [4] are commonly used as threshold angles for FDM, SLS, PolyJet, and SLA, respectively. To print 3D geometry having a greater overhanging angle than the threshold angle, support will be applied and generated. To support these overhanging structures, FDM utilizes breakable or soluble wall pillars, SLS and SLA utilize cylindrical pillars, and PolyJet utilizes solid structure that can be water-jetted or chemically dissolved.

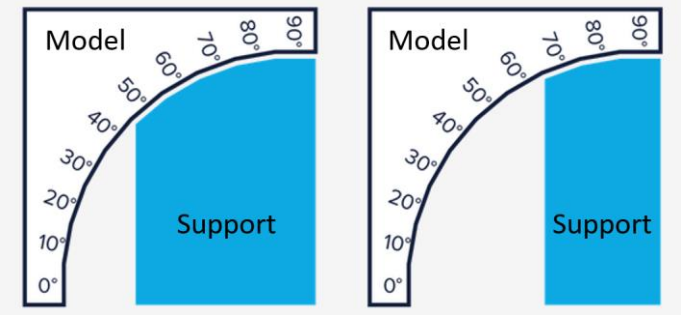


Figure 1: Schematics of overhanging angle (left: 45°, right: 65°)

1.2 Challenges in printing with support structure

All aforementioned supporting approaches; however, have certain limitations for printings with complex geometries due to the nature of postprocessing. Manifolded shells with internal overhanging structure, for example, are virtually impossible to print with any current methods. Similarly, printing of repeated truss structures having small features is another challenge for the current AM processes since support removal tools or dissolvent cannot reach effectively. Although printing process was successfully complete, post processing often causes failures. Chemical support dissolving process can induce expansions of support material due to an absorption of the solvent, which eventually breaks small features and thin walls; mechanical support removing process often damages small features having similar physical size or mechanical strength relative to support structure. In addition, the interface layer at which the model is separated from support tends to exhibit rough surfaces finish or significant dimensional inaccuracy due to material sagging or warpage caused by gravity, material shrinkage, or capillary force. Detachment of model from support is one of the most common failure mode in any AM process that utilizes pillar-shaped support, which has significantly contributed to its unreliability of the current AM processes.

Further, support removal process itself has been a disadvantage of current AM technologies over traditional machining (subtractive manufacturing). Material waste, postprocess labor cost, printing time, are obvious consequences of the printing with excess amount of support. In the actual 3D printing services, the time and labor required for support removal process have been a dominant cost [5]. In addition, printing with dissolvable support material have introduced numerous complexities in the printing process, such as controls, path planning, and cross-contamination between materials, as well as very limited material selection since the combination of wettability, glass transition temperature (Tg), and other mechanical properties are needed to be complementary to each other. In the practical view of AM system design, handling of one extra material for soluble support introduces another degree of freedom in the system; hence, the design and control of the process drastically become complex. All these complexities in the process require tremendousness amount of work to improve the current AM processes.

## 1.3 Existing approaches

To address these challenges related to the AM process with overhanging structure, the use of support structure and material needs to be minimized or ideally eliminated from the process. Self-supporting printing are commonly practiced in commercial FDM machine users to save printing time and materials usage. Since FDM can generate overhanging structure in certain conditions, such as sufficient cooling time per layer and stiffness of entire structure, FDM machine manufactures recommend users to design the model within the overhanging angle of 45 degrees. Also, at horizontal overhanging (*i.e.*, overhanging angle of 90 degrees), bridging technique is frequently applied for small overhanging segments between two structures generated by previous

layers. This method connects two pillars by viscous polymer melt with a rapid cooling and solidification. These methods for non-support printing; however, require design efforts and can successfully generate the desired shape under very limited conditions. For example, material sagging under bridging will be prominent as the length of bridging increases. Also, many thermoplastics commonly used FDM exhibit undesirable material characteristics for the printing processes when rapid cooling is applied. Non-uniform shrinkage and formation of different crystalline are typical challenges for acrylonitrile butadiene styrene (ABS) and poly cyclohexylenedimethylene terephthalate glycol-modified (PCTG), respectively [6] [7]. In addition, various deposition-based self-supported printings processes, photopolymer extrusion [8] and 6-DOF FDM [9] for example, have been also explored. However, the nature of material deposition process that the viscous material is in direct contact with printing objects is a major limitation for the self-supported printing. Printing any structure with some height having similar feature size relative to nozzle size, is impossible to print because the structure does not have sufficient mechanical strength to overcome the force or moment applied on the structure by dragging of viscous materials, such as polymer melts or photopolymers.

Digital geometry processing approaches, such as separation of models, optimization of printing orientation, and minimization of packing area, have been proposed to address the issues associated with overhanging structures. Researchers in Purdue University reported an optimization framework for 3D printing to minimize printing time and support material required to print 3D geometries [10]. This method divides the mesh model into segments at certain locations based on several parameters, including the size of connection area or volume of each segment. Then, these segments are tightly packed to minimize the amount of support and the boundary volume of the packed segments with keeping the minimum number of segments. This proposed frame work;

however, cannot eliminate the use of support completely as well as introducing another postprocessing of assembling by welding or bonding of all segments.

## 1.4 Proposed method and objectives

In this study, a new class of 3D printing approach for self-supported printing is proposed. The concept of the printing process includes jetting of material, instantaneous curing of the jetted material, and selectively repeating the process. For the printing material, ultra-violet (UV) curable polymers (photopolymers) were selected because of its fluidity for jetting and capability for rapid curing. A printing head jets photopolymer and cures the projected photopolymer immediately by an array of UV laser diodes at the intersect with jetted material and focus of the laser array beneath of the jetting orifice. Most importantly, instead of building the 3D object with the conventional layer-by-layer fashion, the proposed printing method draws the toolpath in 3D space using a multi-axis motion stage without contacting with printing objects. This proposed process potentially can generate any complex geometries without support structure and is currently under the patent application (US 62/625,176, Provisional).

The objective of this study is to test the feasibility of this process concept by: designing and construct prototype machine with defining mechanical requirements for the proposed process, characterizing key material properties for the process with establishing an experimental procedure, and investigating a potential modeling approach to optimize the process. This paper outlines the design of mechanical system in Chapter 2, material characterization in Chapter 3, and the process modeling with the results of test printing and discussion are presented in Chapter 4, followed by the summary in Chapter 5.

# 2. DESIGN OF MECHANICAL SYSTEM

## 2.1 Overview

Chapter 2 addresses the development of mechanical designs and its controls required to demonstrate the potential of the proposed printing method. The conceptual design for the 6-axis machine of CAD (Computer-Aided Design) drawing is illustrated in Figure 2. This conceptual configuration visualizes the proposed printing process to create virtually any 3D objects without support. The controls and process developments with multi-axis stage will not be addressed in this study; however, the presented conceptual design is the ultimate goal for the proposed printing method.

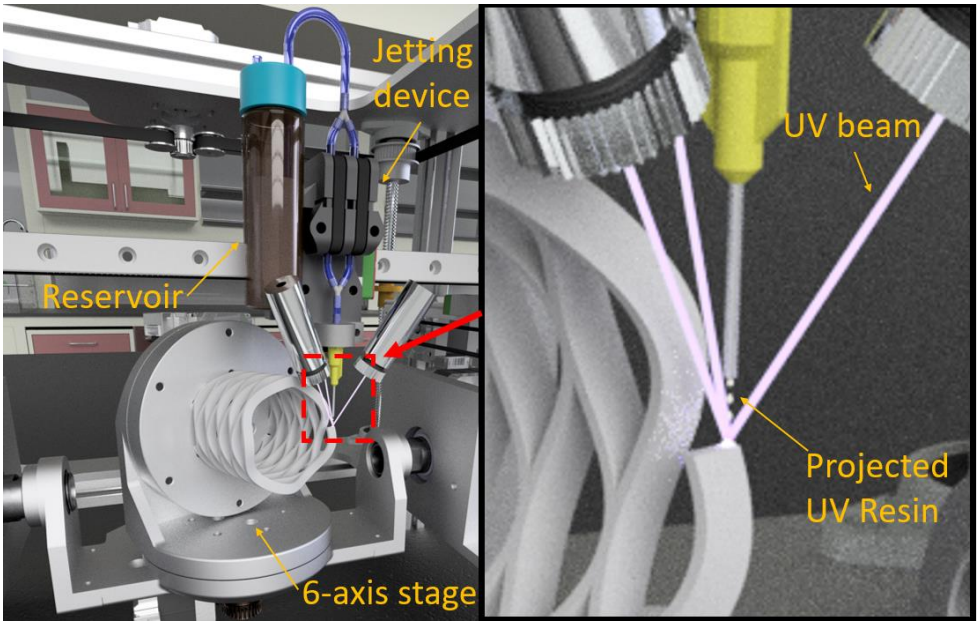


Figure 2: Conceptual mechanical design and process visualization for 6-axis machine

As a proof of concept, a simplified prototype, consisted of a print head and a Cartesian (3-axis) motion stage, was constructed in this study. To ensure the functionality of all major components, the design requirements for the mechanical system were firstly defined as followed;

- Capable to project material having viscosity ranging from 1 to 200 cP at a constant averaged volumetric flow ranging from 0.1 to 0.5mm$^3$/s from single orifice.
- Capable to control material temperature ranging from 25 to 100 °C to condition the material viscosity.
- Capable to apply a point UV light source with Gaussian distribution having 405 nm wavelength aiming a point under the orifice from a distant location.
- Capable to locate the jetting orifice to desired positions relative to printing platform.
- Capable to add multi-axis control for future development

For the material feeding and projection, the viscosity ranges and operational temperatures were determined based on acquired material datasheets. The size of orifice was determined to be 0.1 to 1.2 mm because of its availability of components, such as needles used for applicators or nozzles used for FDM printers. A constant volumetric material flow rate from single orifice is essential for the process modeling analysis; therefore, temperature of material must be controlled within ±1 °C to condition material viscosity since volumetric flowrate of fluid in small orifice may exhibit a dependency on the viscosity of the material. To assume averaged constant volumetric flow rate, the frequency of propelling force (*i.e.*, jetting, gas, or piezoelectric pump) must be continuous or at least 10 Hz with a flow rate ranging from 0.1 to 0.5 mm$^3$/s. The UV light source needs to have a similar diameter (±50%) to the diameter of projected material at a focus point, and to its light profile needs to be normally distributed (Gaussian distribution) in order to simplify the modeling process. Wavelength of 405 nm was determined to be one of design requirements due to its high availability and high absorbance by a variety of commercial photopolymers as well as many existing studies for the photopolymerization process with 405 nm light sources. The focus point

of UV light source needs to be alighted vertically and able to locate under the orifice within 2 to 6 mm. This configuration ensures to achieve a non-contacting printing as well as it eliminates gravitational effects in the process modeling. In addition, for the future development of the machine, the motion stage needs to be designed capable to add a 2- or 3-axis printing platform, which is typically seen in 5- or 6-axis CNC milling machines' configuration for work piece holder as shown the conceptual design.

## 2.2 Print head design

Based on the design requirements, several different designs for print head were considered and tested. To project resins, the Venturi effect (spray with a gas flow), pressure gradient (pump), or combination of these (pump with a gas flow), were considered. One major challenge in the print head design was high viscosity of commercially available photopolymers having viscosity of at least 100 cP. Commercial jetting systems used for common applications, such as ink-jet printer or liquid dispenser, are usually designed for the fluids having similar viscosity with water (1 cP). Although heating photopolymers can drastically reduce its viscosity, most jetting devices have very limited operational temperature range. This design requirements eliminated most commercial jetting systems from the selection. Atomization devices, such as airbrush or any spray devices, were also considered and tested. The use of gas flow effectively propels the polymer resin; on the other hand, atomization decreases the printing resolution due to the inevitable turbulent flows around the orifice. Also, atomization process, which is considered as a mixing of photopolymer with air, drastically slows down or prevents photopolymerization. This phenomenon is called oxygen inhibition, which oxygen in the air reacts with free radicals that terminates chain reactions

of polymerization. Use of inert gas or nitrogen gas is recommended to suppress the oxygen inhibition of acrylate-based photopolymers [11].

The initial design of material dispenser is shown in Figure 3(a). This consists of two micro piezoelectric pumps (*Servoflo* mp6), a material reservoir, a 24-gauge needle (ID = 0.311 mm), and an array of 405 nm laser diodes. A concentric gas channel (ID = 1.7 mm) was added to the actual prototyped dispensing apparatus and shown in Figure 3(b). The compressed air around 6 psi was supplied into the channel to spray since the micropumps used in the experiment did not generate sufficient pressure gradient to jet the viscous resin. In Figure 4, the results of preliminary printing tests with the prototyped dispensing apparatus are presented. This test was manually performed without a motion stage. Although it generates some overhanging structure, the prototype apparatus could not achieve a constant material flowrate or steady state condition. In addition, frequent formation of buildup around the orifice was observed, which is due to some uncertainties of fluid behaviors, such as turbulent flow sounded the orifice or capillarity actions in the concentric gas channel.

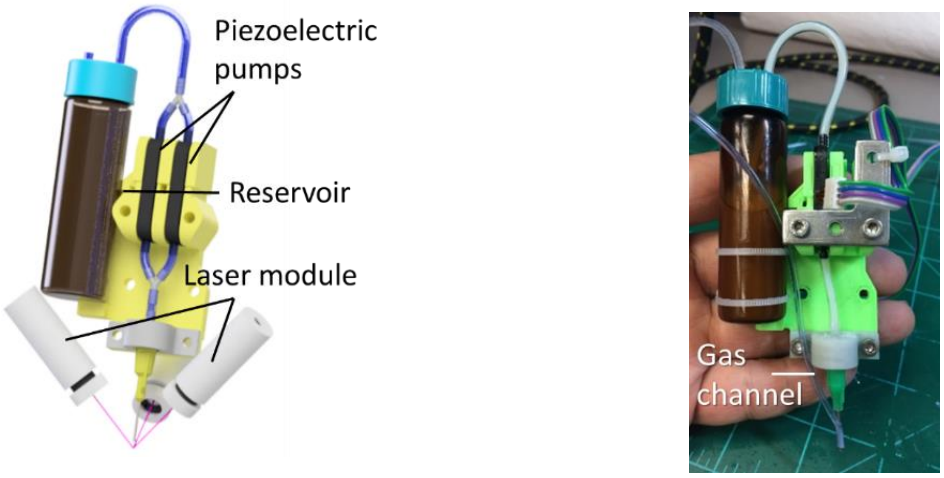


(a) (b)

Figure 3 (a): CAD drawing of the initial print head design (b): prototyped apparatus

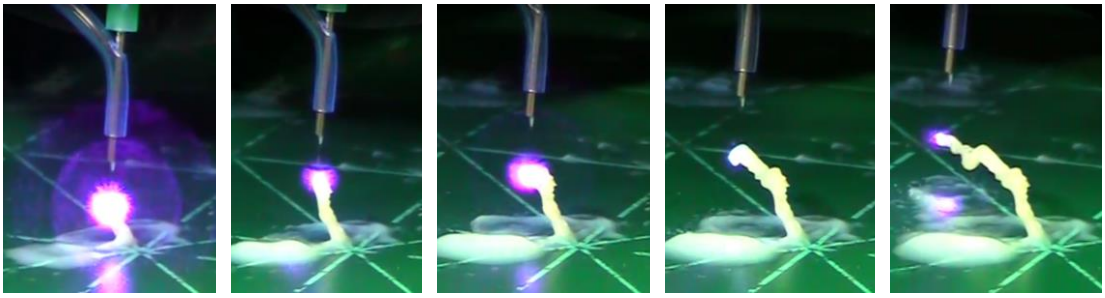

Figure 4: Preliminary printing test with prototyped apparatus (20s, 40s, 50s, 60s, and 80s)

To overcome issues of unsteady condition and the formation of buildup around orifice due to curing of material, a final design of the print head was created, presented in Figure 5(a). Multiple laser modules are attached around the jetting orifice to cure the material at its intersection with the laser beams. The liquid resin is mechanically jetted by a solenoid pin that generates sufficient pressure gradient to create projectile of liquid resins with a certain frequency. The actual system was built in Figure 5(b), which consists of a micro piezoelectric pump (*Servoflo* mp6) for material feeding, an array of 405 nm 50 mW laser diodes (*Sony* SLD3232VF), a 40 W ceramic cartridge heater with a 100 kΩ thermistor for PID temperature controlling, a 12 V solenoid valve with a 0.3 mm orifice for material jetting, and an optical lens array (convex lens and collimating lens) for light conditioning. Figure 6(a) illustrates an exploded view of the jetting mechanism as well as its actuation order is shown in Figure 6(b). The solenoid is firstly actuated to retract the solenoid pin. After material was filled by feeding the resins by the piezoelectric pump, the solenoid pin is released. By repeating this process with a certain frequency, the system controls the volumetric of jetting. Figure 6(c) shows the actual fabricated jetting device. This print head was used for the all tests and analysis in the following chapters.

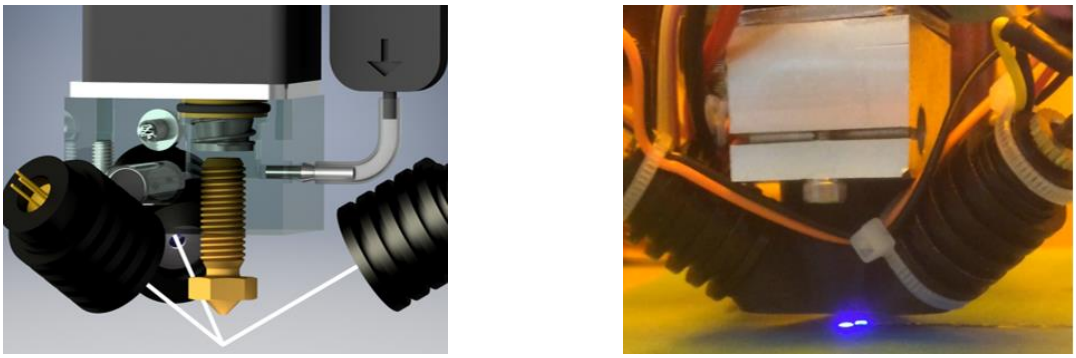

(a) (b)

Figure 5 Final print head design: (a) CAD model and (b) fabricated prototype

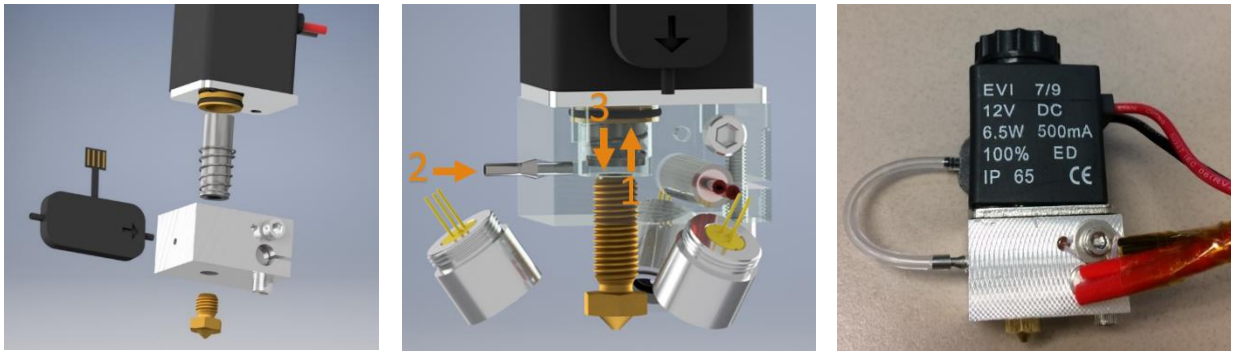


(a) (b) (c)

Figure 6: (a) Exploded view of jetting head (b) actuation schematics (c) fabricated prototype

The optical output, profile diameter, and wavelength distribution of the laser array were measured by a power meter (*Thorlabs* PM100D), a beam profilometer (*Edmunds Optics* Beam profiler 89-308), and a beam spectrometer (*Ocean Optics* USB2000+), respectively. The laser array emitted power of 1.16 mW with diameter of 0.5 mm, and quasi-Gaussian distribution with a peak wavelength of 404nm were observed. Figure 7(a) shows a beam profile of the laser array at approximately 5 mm away from the focus point. These beams converged at a focus point, and successfully generates a circular shape as shown in Figure 7(b). These optical characteristics of the fabricated laser array and results of measurements will be discussed in Chapter 3. One finding in the optical array design was that using a PWM controller to regulate optical power output is not

suited for any laser diodes and its drivers. Any fluctuation of voltage in diodes distorted its beam profile significantly. Hence, it requires a current-based controller to regulate the optical output without distorting the beam profile. In this study, the optical output was fixed for the entire experiments.

(a) (b)

Figure 7: Profile of the laser array: (a) at 5mm away from intercept (b) convergence of beams

2.3 Stage design and controls

A Cartesian stage was constructed for the translations of the designed print head. A schematic is presented in Figure 8(a). This stage consists of five stepper motors (*Kysan* Nema17 1124090), a set of linear motion sliders (MGN12) and 200 mm leadscrews (T8), a belt drive system (GT2 6mm), a set of 2020 aluminum extrusion frames, a set of amber polycarbonate panels, and 3D-printed fixtures. The print head is attached to the carriage that has 3 degrees of freedom. This configuration allows the print platform to be stationary so that a 2- or 3-axis printing platform can be added for further development. An *ArduinoMega*-based integrated board (ATmega2560), *RUMBA*, was selected as a main control board. A opensource 3D printing firmware, called *Marlin*, was utilized as a toolpath (Gcode) interpreter to control all actuators and sensors simultaneously. Two stepper motors were coupled and synchronized to actuate y-axis and z-axis while single

stepper motor drives x-axis. Each stepper motor was connected to *Trinamic* TMC2100 stepper drivers, providing noiseless current controls to attenuate vibrations due to stepping of motors. GT2 6mm width belt drive system and 4 sets of 8mm leadscrew system were used to transmit the mechanical input from stepping motors to the linear motion of the individual axis. The fabricated prototype is shown in Figure 8(b). A 12V 150 W heating element was installed on a 200 mm × 200 mm × 3 mm aluminum sheet, used as a print platform, to maintain the temperature of resin during the printing process. Also, painting masking tape was applied on the platform surface to suppress the reflection of laser beams that causes buildup around orifice.

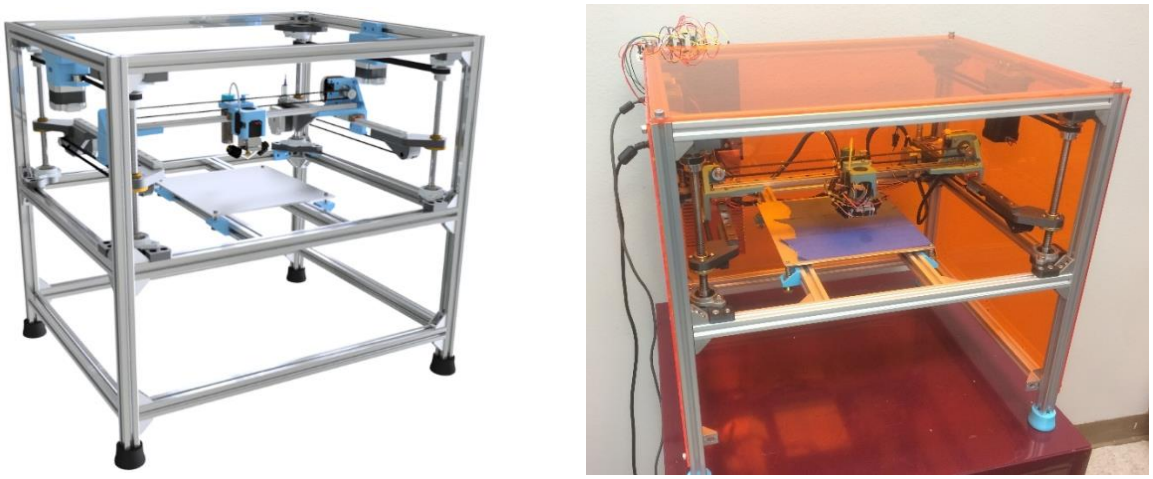

(a) (b)

Figure 8 Overall design of prototype machine: (a) CAD drawing and (b) fabricated machine

To control the flowrate of the printing head from Gcode, stepping signals for FDM extruder was utilized to actuate solenoid pin that jets the resins. By experimentally identify the jetting volume per stroke of solenoid pin, a desired amount volume can be precisely controlled from Gcode via stepping signal. A sample calculation for stepping signal of FDM process is shown Equation 1, assuming a stepping motor having 1.8 degree per step, extruder gear having 4 mm radius ($R_{extruder}$), and no micro stepping. This calculated value is used when Gcode interpreter

converts feed rate into actual rotation of FDM extruder, which feed rate is calculated by toolpath planner (slicing software for 3D printing) for desired volumetric flow with a certain filament size. The calculate stepping size was then converted to the volume per stroke by conducting calibration of print head, measuring a volumetric flow at a certain period with a constant stroke frequency. In Equation 2, the calculation for the conversion factor is shown, based on a calibrated volumetric flow per stroke of solenoid pin and assuming Gcode is prepared with 1.75mm filament. The converted signal was send to a 12V metal-oxide-semiconductor field-effect transistor (MOSFET) to actuate solenoid pin instead of sending to a stepper driver. This control scheme allowed to create a low cost integrated control system for the proposed printing process without developing any customized control system.

$$\frac{1\ step}{1.8\ °} \times \frac{16\ signals}{1\ step} \times \frac{360\ °}{1\ rev} \times \frac{1\ rev}{2\pi R_{extruder}} = 127.32 \frac{signals}{mm} \quad (1)$$

$$0.03 \frac{mm^3}{stroke} \times \frac{stroke}{\pi R_{filament}{}^2 \times 2\pi R_{extruder}} = 9.93 \times 10^{-4} \quad (2)$$

## 2.4 Results and discussions

The constructed prototype was experimentally evaluated by performing a series of tests. Figure 9(a) shows a result of jetting performance test without applying UV-light source. A quasi-constant jetting profile was maintained up to 8 mm of jetting distance, and the frequency of 15 Hz was the limit of the actuation of solenoid pin for a steady state flow. Reducing viscosity of resins by applying heats were effective to attain a constant flow rate as well as it facilitated the faster actuation of solenoid pin. Figure 9(b) shows a result of material curing test for jetted material without motion stage. The material flow rate of this jetting device was estimated by measuring the

mass flow rate of the jetted material and converting it to a volumetric flow with assuming isochoric condition. With 15 Hz of actuation of solenoid pin, the averaged measured flowrate was 0.5 ± 0.2 $mm^3/s$ for a material viscosity of approximately 50 cP with heating, which viscosity data will be presented in the next chapter. Some inconsistencies were observed in the volumetric flow measurement. This might be explained by the fact that the volumetric flow is calculated from mass measurements, which does not consider thermal expansion of liquid resins. One observation that the volumetric flow becomes more consistent when the entire system reaches steady state temperature (*i.e.*, when platform temperature and inside of chamber were heated long time) indicated the significance of temperature effect to attain a consistent jetting flowrate. Heating the material reservoir and the entire material feeding path need to be considered for the next iteration of print head design.

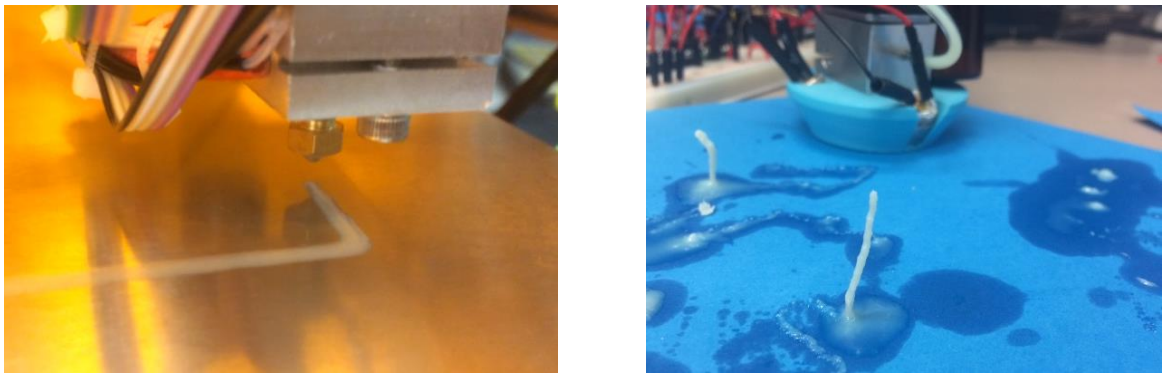

(a) (b)

Figure 9: (a) Jetting test without curing (b) preliminary print test without motion stage

One limitation found in the system was that the actuation of solenoid pin has a limited frequency range. Below the actuation frequency of 15 Hz, the flowrate showed a moderate linearity with respect to the actuation frequency; however, no correlation was found above 25 Hz. This is resulted from the mechanical resonance or aliasing when the pin cannot overcome the viscosity of resin to travel with the given velocity. Applying higher power on solenoid, of course, will help the

faster actuation of the pin. However, the design that the solenoid pin is submerged into the resin appears the dominant cause of the limited frequency range. The surface area of solenoid pin contacting with viscous resins should be reduced for the next design of the print head.

## 2.5 Conclusions

The mechanical design required for the proposed printing method was investigated in this chapter. Based on the defined design requirements, a prototype was designed and prototyped. Although the results of testing indicated some limitations, the constructed prototype proved to possess sufficient capabilities for the proposed printing process by satisfying design requirements. A maximum flowrate of $0.5 \pm 0.2$ $mm^3/s$ was achieved with 15 Hz of actuation of solenoid pin and material viscosity of approximately 50 cP by heating. This prototyped machine will be used for printing test to verify a process model addressing in Chapter 4. To summarize this chapter, the specifications of the constructed prototype are presented in Table 1.

Table 1: Specifications of the constructed prototype machine

| | Quantity | Unit |
|---|---|---|
| Maximum flowrate | $0.5 \pm 0.2$ | $mm^3/s$ |
| Maximum actuation frequency | 15 | Hz |
| Jetting resolution | 0.03 | $mm^3/s$ |
| Orifice size | 0.3 | mm |
| Maximum jetting distance | 8 | mm |
| Laser array optical output | 0.8 | mW |
| Laser profile diameter | 0.5 | mm |
| Peak wavelength | 404 | nm |
| Print volume | 200 × 200 × 145 | mm |
| x-y axis mechanical resolution | 0.050 | mm |
| z axis mechanical resolution | 0.025 | mm |
| Maximum speed in x-y direction | 200 | mm/s |

# 3. MATERIAL CHARACTALIZATION

## 3.1 Overview

This chapter discusses and identifies the material properties of photopolymers for the proposed printing process. To determine proper ranges of the printing speed by creating a process model, the photopolymer optical and physical properties need to be characterized prior to use. Experimental procedure and its setup for the determination of the photopolymers' properties also need to be established to obtain consistent results. Optical characteristics of the designed laser optical array in the previous chapter is examined to quantify the system parameters required to model the process. In this study, four commercially available photopolymer resins are selected. These photopolymers' governing key parameters with 405 nm wavelength light source are identified by conducting a series of experiments. Temperature dependency of the photopolymerization and physical properties of resins are investigated in this chapter.

## 3.2 Jacob's model: windowpane test and working curve method

Jacobs' model [12], used in conventional vat polymerization processes, such as SLA or digital light processing (DLP), was utilized to determine the two key parameters governing the photopolymerization: critical exposure ($E_c$) and penetration depth ($D_p$), which depend on the resin's absorbance characteristics [13]. Penetration depth is defined as the depth of resin at which reduces the irradiance to $1/e$ (approximately 37%) of the maximum irradiance at the surface. Assuming a Gaussian distribution and symmetric profile, illustrated in Figure 10, the laser irradiance can be expressed as Equation 3, where $H_o$ is the maximum irradiance based on the laser

power ($P$), defined by Equation 4, $C_d$ is the measured curing depth of the resin, and $w_0$ is the radius of the laser beam.

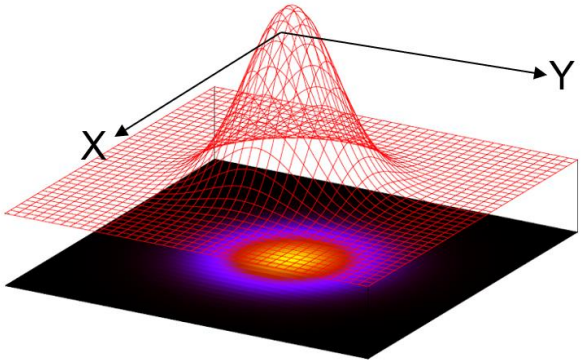


Figure 10: Visualization of Gaussian irradiance distribution and light profile

$$H = H_o e^{-C_d/D_p - 2y^2/{w_o}^2} \quad (3)$$

$$H_o = \frac{2P}{\pi {w_o}^2} \quad (4)$$

Since photopolymerization depends upon the number of actinic photon absorbed per unit volume, this energy can be quantified as the exposure ($E$) that can be derived by integrating irradiance over the time. Assume the laser is being scanned at a constant velocity ($v$), which can be written as Equation 5. By substituting this into Equation 3 and solving the given differential equation, it yields Equation 6, which is the exposure applied on the resin having the units of energy per unit area (*i.e.*, $mJ/cm^2$). Since the exposure reaches its maximum value at when $y = 0$ (*i.e.* center of the scanning axis) and $z = 0$ (*i.e.* surface of resin), the maximum exposure ($E_{max}$) can be written as Equation 7.

$$v = dx/dt \;\; or \;\; dt = dx/v \quad (5)$$

$$E = \sqrt{\frac{2}{\pi}} \frac{P}{w_0 v} e^{-C_d/D_p - 2y^2/{W_o}^2} \quad (6)$$

$$E_{max} = \sqrt{\frac{2}{\pi}} \frac{P}{w_0 v} \quad (7)$$

Photoinitiators in acrylate-based photopolymers will generate free radicals to create chain reaction of polymerization when sufficient exposure is applied, and this threshold value of the exposure is defined as the critical exposure ($E_c$). This can be determined using the working curve method, so-called windowpane test, as expressed in Equation 8. Figure 11(a). visualizes an idealized profile of a cured photopolymer. Samples were prepared by applying a light source from the top a slide glass that covers a vat filled by a photopolymer resin. The exposure is inversely proportional to the scanning speed; therefore, amount of energy absorbed in the resin can be incremented as the scanning speed is decremented, and vice versa. Figure 11(b) is a typical Jacob's working curve that measured cure depth is plotted with respect to the exposure in semi-log scale [14]. The slope of the working curve is the penetration depth, and critical exposure can be obtained by rearranging Equation 7 and Equation 8.

$$C_d = \begin{cases} D_p \ln\left({E_{max}}/{E_c}\right), & E_{max} > E_c \\ 0, & E_{max} < E_c \end{cases} \quad (8)$$

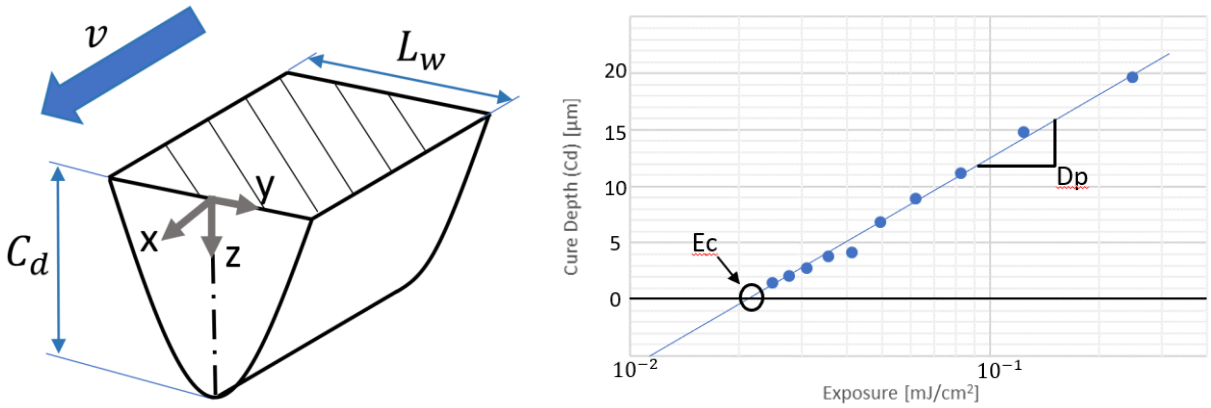


(a) (b)

Figure 11: (a) Schematic of moving windowpane test (b) a sample Jacob's working curve

Some relationships between system parameters can be derived by defining boundary conditions or rearranging the given equations. The maximum cured line width ($L_w$), which will occur at the resin surface, can be obtained by setting $y = L_w/2$ and $z = 0$, shown in Equation 9. However, this equation tends to show large deviations from the actual measurements. This is due to natures of fluid (surface tension or capillarity), light (reflection or scattering), assumptions (Gaussian or $1/e$), or kinetics of photopolymer (random radical motions). In addition, the required laser scanning speed can be estimated by Equation 10 for the known critical exposure and the penetration depth values, which is used in conventional vat polymerization processes.

$$L_w = W_0 \sqrt{\frac{2C_d}{D_p}} \qquad (9)$$

$$v = \sqrt{\frac{2}{\pi}} \frac{P}{w_0 E_c} e^{-C_d/D_p} \qquad (10)$$

The critical exposure and penetration depth may have some temperature dependency because the thermal energy in the polymer molecules have strong correlation with kinetics of free radicals [15]. The temperature dependency of the photopolymerization will be investigated in the following

chapter as well as the temperature dependency of the physical properties, such as viscosity and density. Another key characteristic of photopolymer is resin's viscosity. Arrhenius' viscosity model [16], shown in Equation 11, describes the relationship between viscosity ($\mu$) of resin and its temperature ($T$), where $\mu_0$ is coefficient, $E$ is activation energy (J/mol), and $R$ is gas constant of 8.314 J/mol-K.

$$\mu(T) = \mu_0 exp\left(\frac{E_a}{RT}\right) \quad (11)$$

3.3 Experimental methods

To quantify the material properties defined in the prior chapter, a series of experiments was conducted. Only light source having wavelength of 405 nm was used for the experiments due to its high availability and high absorbance of commercially available photopolymer resins. An optical array (Figure 12(a)) consisted of a convex lens, collimating lens, an iris diaphragm, and a 50mW 405nm laser diode (*Sony* SLD3232VF) were created to attain an ideal beam profile (Gaussian distribution) that is required for the windowpane test. Figure 12(b) shows a measured beam profile of the created optical array, having an effective diameter of 0.5 mm, by a beam profilometer (*Edmunds Optics* Beam profiler 89-308). The distribution was not an ideal distribution; however, the beam profile was sufficient to assume as a Gaussian distribution only for the moving path windowpane test. The optical output of the single laser array was measured by a power meter (*Thorlabs* PM100D), and was 0.388 mW. The wavelength spectrum of the optical array, measured by a beam spectrometer (*Ocean Optics* USB2000+), is presented in Figure 13. A peak wavelength of 404nm was observed in the spectrum.

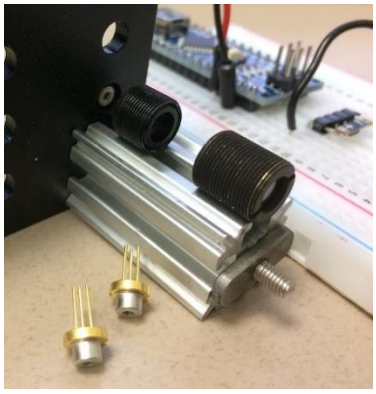

(a)

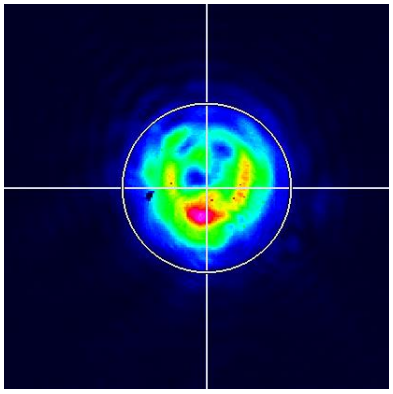

(b)

Figure 12: (a) laser array components (b) measured beam profile (D = 0.5 mm)

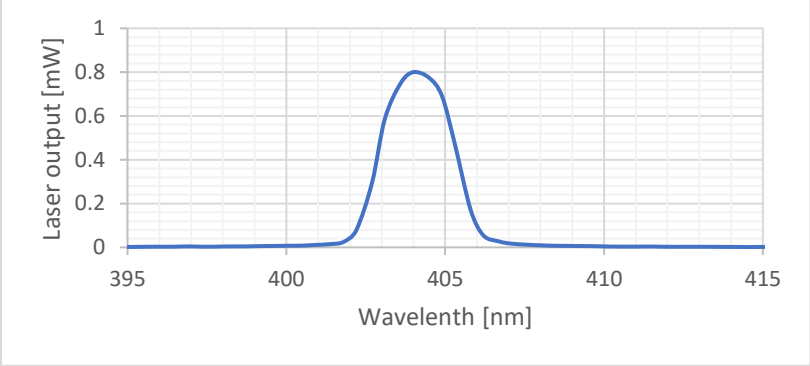


Figure 13: Measured wavelength spectrum of the optical array

Four commercially available photopolymer resins, VeroWhitePlus (RGD835), TangoBlackPlus (FLX980), and HighTemperatureWhite (RGD525) were obtained from *Strata-sys* Ltd. (Eden Prairie, MN, USA) as well as MakerJuice G+ (Hard Multi-Purpose Resin) from *MakerJuice Lab* for this study. The laser beam was applied with a constant feed rate at a fixed distance, at which the beam profile was measured, from the liquid resin surface. The experimental setup for the windowpane test is shown in Figure 14(a). A 20 × 20 × 10 mm container was filled by the photopolymer resin, and a slide glass having a thickness of 0.1 mm was placed over the top of the container that is in direct contact with the photopolymer. The resin was replaced for each sample preparation to prevent any hysteresis due to the exposure applied by previous sample

preparation. Figure 14(b) shows the overview of the experiment setup. The laser was scanned along x-axis with alternated pattern with different scanning speed. An example of the tool path is illustrated in Figure 15. The temperature of the resin is recorded for each sample by a thermocouple. Figure 16 shows an example of a sample for RGD835 at 22.1 °C with scanning speed of 200, 300, 600, 900, and 1,200 mm/min. The prepared samples were cleaned with isopropyl alcohol to prevent further curing of residual material on the sample before the curing depth measurements.


(a) (b)

Figure 14: (a) motion stage for the windowpane test (b) sample preparation

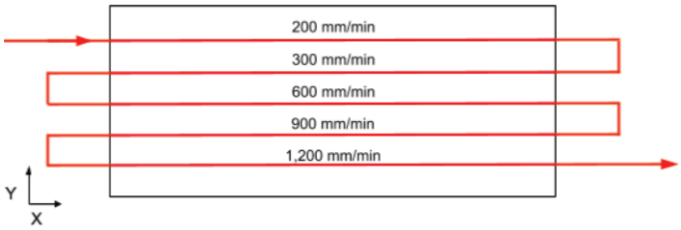


Figure 15: An example of a toolpath used for sample preparations

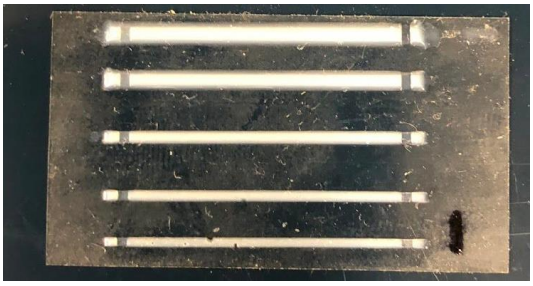

Figure 16: Prepared sample with RGD835 at 24.0 °C

A digital microscope (*Keyence* VHX-600K) with a vertical fixture, shown in Figure 17(a), was used to measure curing depth of samples. An example of measurement is shown in Figure 17(b). With a sample size of at least 5 per applied exposure with 95% confidence level, the estimated

uncertainty (standard error of mean) of the cure depth measurement for RGD825 was between from ±0.02 mm to ±0.04 mm depending on applied exposure, which are between 2.4 % to 4.8 % of error. In addition, a sample measurement for the line width at the bottom (*i.e.*, at the glass slide surface) is shown in Figure 17(c). The width of the sample at the curing height of 37% ($1/e$) was also recorded to verify the line width relationship described in Equation 9.

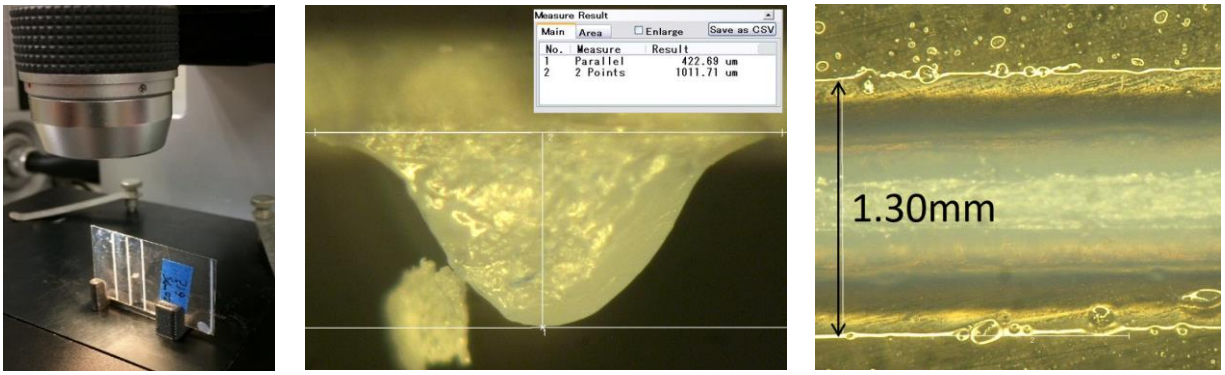


(a) (b) (c)

Figure 17: (a) $C_d$ measurement setup (b) $C_d$ measurement (c) linewidth measurement

The temperature dependency of photopolymerization process and material viscosity were also investigated to condition jetting process and its effects on materials' photopolymerization characteristics. Figure 18 shows the material vat with a heater used for the windowpane test with various temperature. A PID controlled 200 W heater was attached to the backside of the material vat and a thermocouple is directly in contact with photopolymer resins to measure the resin's temperature at the center of the resin vat. For each measurement, the temperature of resins was stabilized for at least 5 minutes before applying the laser beam. For the viscosity measurement, a viscometer (*Hydromotion* Viscolite700) was utilized, and the setup is shown in Figure 21.

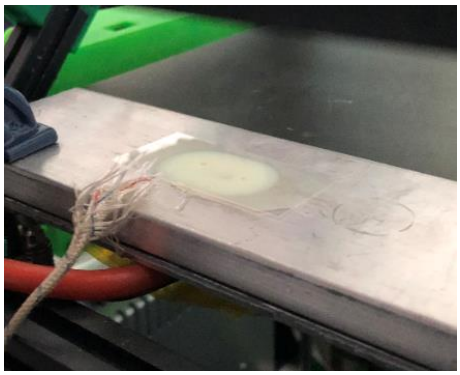

Figure 18: Material heater with thermocouple

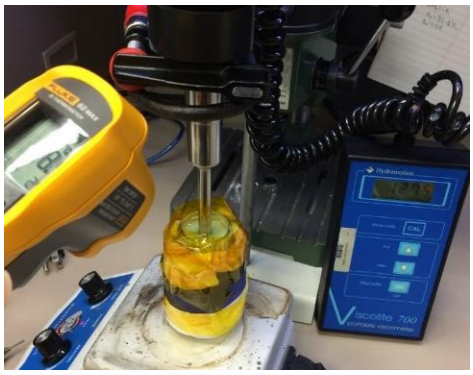

Figure 19: Viscosity measurement setup

3.4 Results and discussions

Following the procedure in Chapter 3.3, the obtained working curves for RGD835 and FLX980 resins at room temperature are presented in Figure 20 and Figure 21. Penetration depth and critical exposure were determined to be 0.165 mm and 1.19 mJ/cm$^2$ for RDG835, and 0.214 mm and 5.41 mJ/cm$^2$ for RDG835. While RGD835 showed closer penetration depth and critical exposure with the reference values, which was within 14 % for penetration depth and 37% for critical exposure, FLX980 exhibited significant differences from the existing study; 40 to 31% difference was observed between the obtained critical exposure and the reference values [17]. Major error source in FLX980 measurement is the its low stiffness (shore A 26-28) [18] and high elasticity that caused some complexities in the sample preparation, such as detachment of samples from the slide glass or sample distortion during the cleaning process. Also, the high absorbance of the FLX980 as observed in its high critical exposure may indicate time dependency; the motion of free radicals may create wider and flatter curing profile when the high power was applied. This possible time dependency needs further investigation. Another known issue in photopolymer characterization process was that photopolymers exhibited wide ranges of variation between the production batches. These uncertainties in the material characterization process needs to be considered in the process

model as a safety factor. Results for the other photopolymers are presented in Figure 22 and Figure 23, and obtained results for the curing parameters for all four photopolymers are summarized in Table 2.

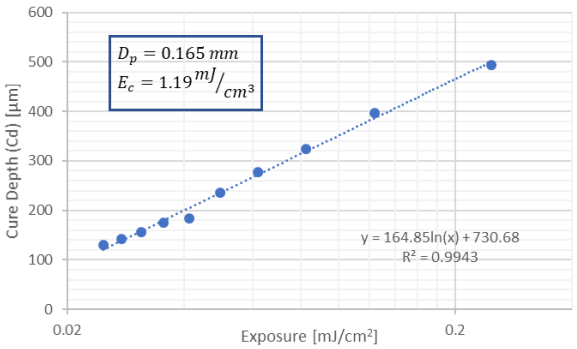


Figure 20: Working curve for RGD835 (VeroWhitePlus) at 25 °C

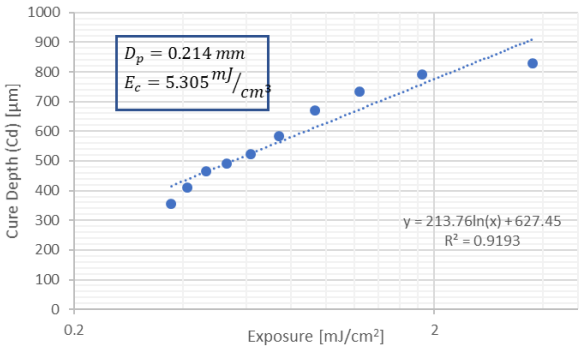


Figure 21: Working curve for FLX980 (TangoBlackPlus) at 25 °C

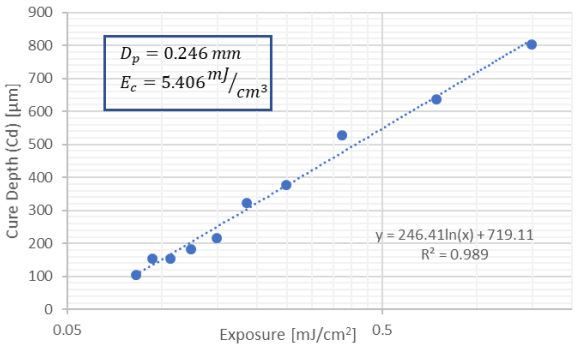


Figure 22: Working curve for MakerJuice G+ at 25 °C

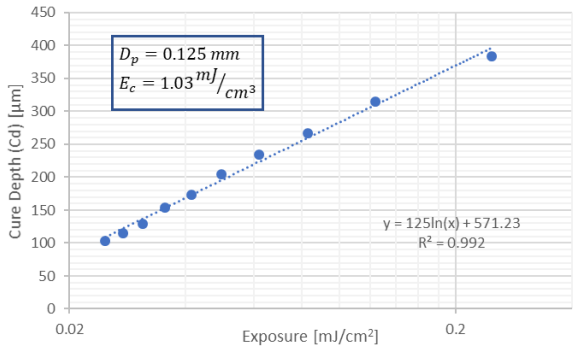


Figure 23: Working curve for RGD525 (HighTemperatureWhite) at 25 °C

Table 2: Measured curing parameters at 25 C° for 405 nm laser

| | **RGD835** | **FLX980** | **RGD525** | **G+** |
|---|---|---|---|---|
| $\boldsymbol{D_p}$ $\boldsymbol{[mm]}$ | 0.165 (0.145)[Ref] | 0.214 (0.151)[Ref] | 0.125 | 0.247 |
| $\boldsymbol{E_c}$ $\boldsymbol{[mJ/cm^2]}$ | 1.19 (1.9)[Ref] | 5.35 (4.1)[Ref] | 1.04 | 5.41 |

Figure 24 presents the measurement of viscosity of RGD525 with various temperatures. Significant changes in viscosity were observed; viscosity was drastically decreased from 253 cP to 14 cP as temperature increases from room temperature to 90 °C. The result suggested the importance of the temperature control for the jetting process to attain the constant jetting flowrate. However, some local material curing was observed above 70 °C at the bottom of the resin vat that was potentially induced by the heat. For RDG525, between 40 and 60 °C was determined to be the ideal temperature range for the process with a safety factor. Lastly, Arrhenius's model (Equation 11) was applied to the obtained data for RGD525 (Figure 25). Activation energy and coefficient were 39.6 kJ/mol and $2.3\times10^{-5}$, respectively.

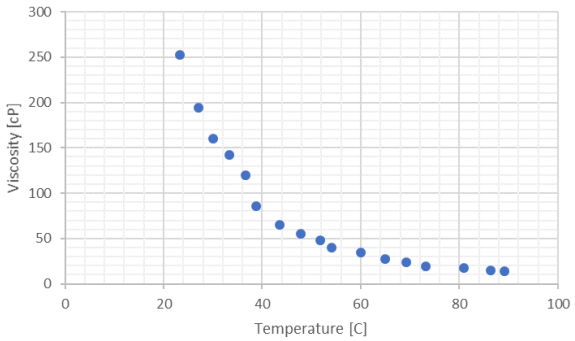


Figure 24: Measured viscosity of RDG525 (HighTemperatureWhite)

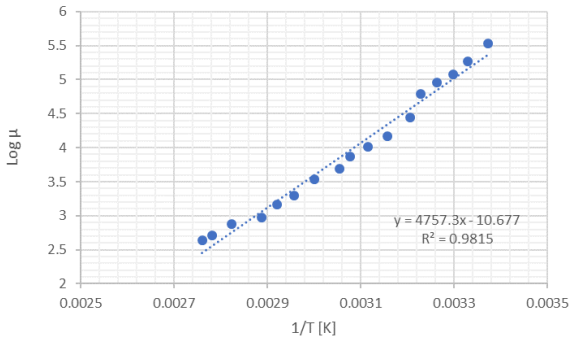


Figure 25: Fitted Arrhenius' viscosity correlation for RDG525

In Figure 26 and Figure 27, the penetration depth and critical exposure of RGD835 resin with respect to temperature are presented. These results did not indicate significant temperature dependency of the photopolymerization within the temperature range for jetting process determined by the previous viscosity measurement. The variation between data points were within the range of the experimental uncertainty; any correlation was not captured. Although the kinetics of the radicals can be promoted by absorbing thermal energy that will facilitate the photopolymerization, other uncertainties in the process, such as the difference between material

batch, light exposure history of the material, heat gradient in the sample, or time dependency of the photopolymerization, will be dominate error sources for the process design.

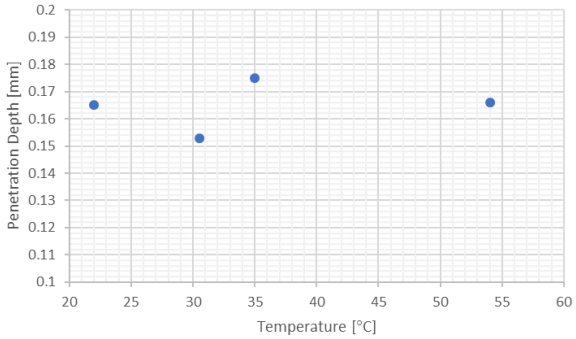


Figure 26: Temperature dependency of the penetration depth of RDG835

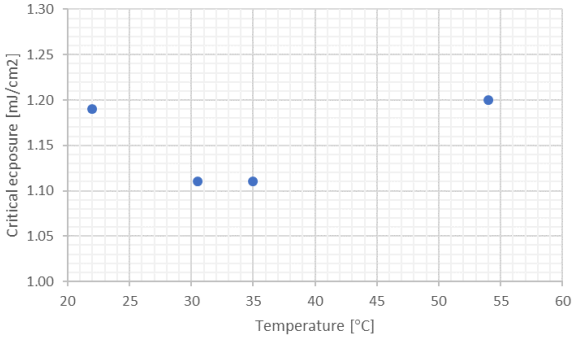


Figure 27: Temperature dependency of the curing depth of RDG835

## 3.5 Conclusions

In this chapter, the parameters of the photopolymers for the proposed printing were identified and quantified. The optical characteristics were firstly determined; single optical array designed in the previous chapter has the beam diameter of 0.5 mm, optical output of 0.388 mW, and peak wavelength of 404 nm. For this optical array, two governing key parameters, penetration depth and critical exposure, for the four photopolymers were identified by conducting moving path windowpane tests, based on Jacob's model. The experimental setup showed consistent results within 2.4 % to 4.8 % errors in curing measurements. 14 % to 41 % errors from reference values were observed, and these errors could be explained by the fact that the photopolymers' production has significant deviation between batches. Temperature dependency of the photopolymerization and viscosity were also investigated. It was confirmed that the viscosity of the material can be estimated by Arrhenius relationship, and photopolymers have limited temperature range for heating due to curing induced by the heat. No strong correlation between temperature and

photopolymerization were observed within the range that these photopolymer resins can be heated. These obtained results will be utilized for the process modeling in the following chapter.

# **4.** PROCESS MODELING

## 4.1 Overview

In this chapter, a process model for the proposed printing method will be presented. This model correlates parameters for the designed process determined in previous chapters, such as jetting flowrate, optical characteristics, or material properties. The model is essential to predict the range of system parameters or variables to control the printing feature size (*e.g.*, width, height, etc.) whereas ensuring the curing of the photopolymers. Particularly, the range of the printing speed (*e.g.*, feed rate of the print heat carriage) for complete curing of material and its generated geometry feature size can be predicted and simulated by the model. The simulated results will be compared to the actual printing process to verify the feasibility of the model. Lastly, the performance of the created prototype will be assessed by conducting a series of preliminary printing experiments to conclude this study.

## 4.2 Parameters identification

To model the process of the proposed printing method, system parameters, material properties, and assumptions were firstly clarified. Table 3 lists the material properties and representing symbols with its relationships discussed in Chapter 3. Note that $D_p$ and $E_c$ has dependency on the wavelength of the light source. Only 405 nm wavelength laser diodes were used in this study due to its high availability and high absorbance of commercial photopolymer resins. Table 4 lists the system parameters for the concept of the designed process. Assumptions are: 1) laser scanning velocity is constant, 2) curing depth (height) is relatively small, 3) material flow is always parallel

to the direction of gravity, and 4) laser profile has a Gaussian distribution. In addition, although the flow rate of the jetting system can be controlled as a function of actuation frequency of the solenoid pin and material viscosity, the model only uses maximum flowrate of 0.5 mm/s$^3$ as a simplification to reduce uncertainty from the flowrate errors discussed in Chapter 2.

Table 3: Material properties

| Parameters | Symbols | Relationships |
|---|---|---|
| Penetration depth (at 405nm) | $D_p$ | Jacob's model (Beer-Lambert Law) |
| Critical exposure (at 405nm) | $E_c$ | Jacob's model (Beer-Lambert Law) |
| Viscosity | μ | Arrhenius equation |

Table 4: System parameters

| Parameters | Symbols | Values / Relationships |
|---|---|---|
| Radius of laser beam | $w_0$ | 0.5 mm |
| Incident power | $P$ | 0.388 mW per unit |
| Material volumetric flow | $\dot{Q}$ | 0.5 mm$^3$/s |
| Printing speed | $v$ | Process model |
| Geometry size | $R$ | Process model |

4.3 Deposition model

The material deposition model for the jetting system is constructed as shown in a schematic in Figure 28. The deposited structure is assumed to be a perfect cylinder along the printing direction, shrinkage due to curing is negligible (volume is conserved), and no jetted material is wasted. The geometry feature size ($R$) can be related to a differential volume (Equation 12). The differential length ($dL$) can be written as Equation 13, where $dz \neq 0$. This is important for the control perspective because each components of differential length ($dx$, $dy$, and $dz$) directly correlates with the control signals for displacement per given time. By using the calculated stepping size and

conversion factor (Equation 1 and 2), the system can produce exact intended motions by traditional toolpath language (Gcode). By differentiating this relationship with respect time, it yields the relationships between the geometry feature size, constant volumetric flow rate ($\dot{Q}$) and printing speed ($v$) as shown in Equation 14. This equation predicts the geometry feature size with a given steady state flow rate as a function of printing speed as well as offering a great controllability of the system by implementing conventional machine control schemes.

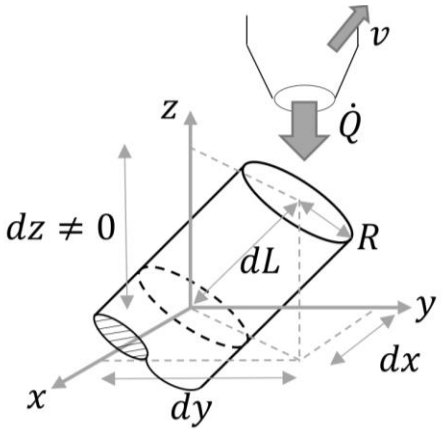


Figure 28 Schematic description of material depositing process model

$$dV = \pi R^2 dL \quad (12)$$

$$dL = \sqrt{dx^2 + dy^2 + dz^2} \quad (13)$$

$$\frac{dV}{dt} = \dot{Q} = \pi R^2 \frac{dL}{dt} = \pi R^2 v \quad (14)$$

4.4 Curing model

The curing model with its criteria was created for the defined geometric feature size by adapting the Jacob's model discussed in Chapter 3.2. The schematic of the process model is shown in Figure 29. Assumptions are followings; radius of laser beam is greater than the geometry size (*e.g.*, $w_0 > R$), the polymerization occurs at the center of each laser beam, and the newly deposited

resin receives only half of the Gaussian irradiance. Since laser is applied from multiple angles radially towards the cylinder, the cylindrical shape can solidify if the curing depth from each laser beam exceeds the predicted radius (*i.e.*, $C_d > R$). In this case, the maximum exposure becomes half of that in Equation 7 (*i.e.*, $0.5E_{max}$), shown in Equation 15. By substituting Equation 15 into Equation 8, the curing depth can be derived as a function of printing speed, shown in Equation 16. This equation is useful to predict the designed process with ensuring complete curing of the material for the given geometry feature size.

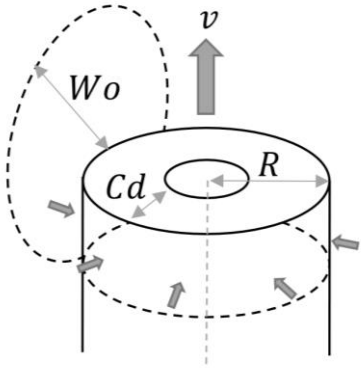


Figure 29 Schematic description of the curing model with laser irradiance range

$$E_{max.half} = \sqrt{\frac{1}{2\pi}}\frac{P}{w_0 v} \quad (15)$$

$$C_d = D_p \ln\left(\frac{P}{\sqrt{2\pi} w_0 v E_c}\right) \quad (16)$$

4.5 Implementation of process model

For the simulation and actual printing tests, constant flowrate of 0.5 $mm^3/s$, optical power of 0.78 mW (2 units of optical arrays) with a beam diameter of 0.5 mm, and obtained penetration depth and critical exposure values were used. In this case, only variable to be controlled is printing speed. With these parameters, the predicted curing process for FLX980 is plotted in Figure 30

using Equations 14 and 16, based on its properties. This plot can be interpreted that $C_d$ exceeds $R$ when the printing speed is between 0.2 and 6 mm/s, which indicates the range of the printing speed for the curing depth criteria. Also, the geometry feature size needs to be equal or less than beam diameter. Hence, this plot can be inferred that the proper printing speed range is between 0.8 and 6 mm/s. The results of simulation for RGD835, RGD525, and MakerJuice G+ are plotted in Figure 31, Figure 32, and Figure 33, respectively.

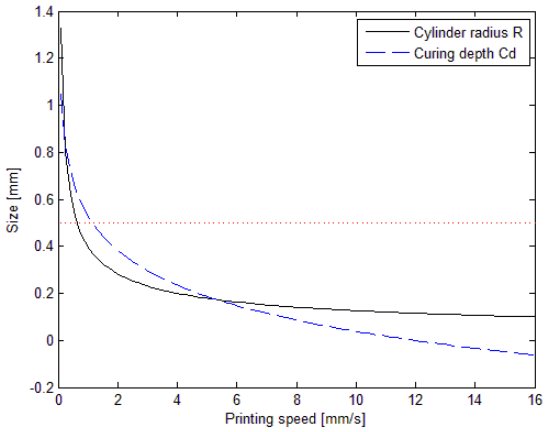


Figure 30: Simulated feasible printing speed for FLX 980 (0.6 to 6 mm/s)

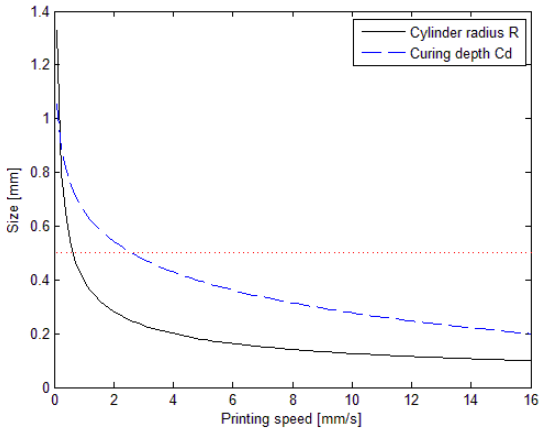


Figure 31: Simulated feasible printing speed for RGD 835 (0.6 to 34 mm/s)

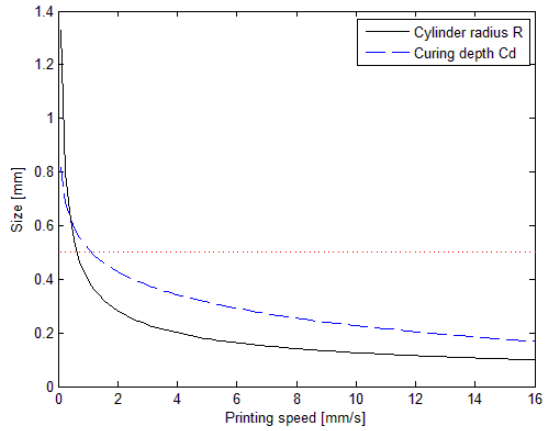


Figure 32: Simulated feasible printing speed for RGD 525 (0.6 to 35 mm/s)

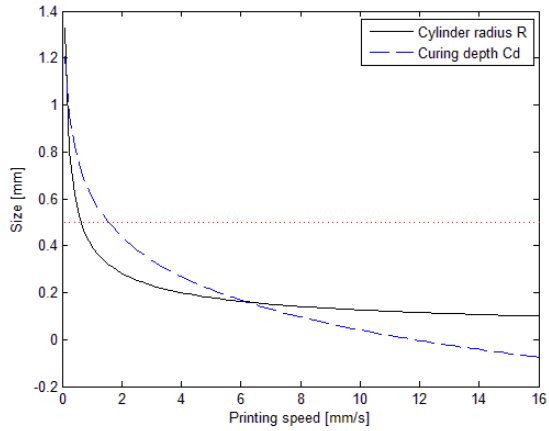


Figure 33: Simulated feasible printing speed for MakerJuice G+ (0.6 to 6 mm/s)

## 4.6 Results and discussion

To validate the proposed model, a series of printing tests was conducted. A conservative printing speed of 1.0 mm/s was used since this speed was expected to work for all four materials. To test the repeatability of the overhanging structure printing, a 50 mm structures with a single pass were printed with various overhanging angles. Also, maximum overhanging capability was tested by creating a single path printing test with gradually incrementing of the overhanging from 0˚ to 90˚ degrees. All tests were printed in y-z-direction since two units of laser array was applied along the x-direction while the printing head was fed along the y-z-plane.

The selected printing speed was able to successfully cure the material as predicted. However, FLX980 began to collapse after it reached 2-3 mm height and did not complete the print due to the low stiffness (shore A 26-28) compared to the other three materials (shore D 75 to 88) [18] [19]. All other materials showed noticeable support-free capabilities up to 90˚. Figure 34 illustrates a self-supported print of a 60˚ overhanging structure by a single pass with RGD 835. The cured radius was approximately 0.5 to 0.6 mm, whereas the predicted radius was 0.4 mm (Equation 14). Although the structure is formed properly, an uneven surface finish can be observed due to the fusion of droplets with rapid curing, which could explain the discrepancy between the predicted geometry size and measured size. In addition, gravity and liquid surface tension may also play a role in structure uniformity.

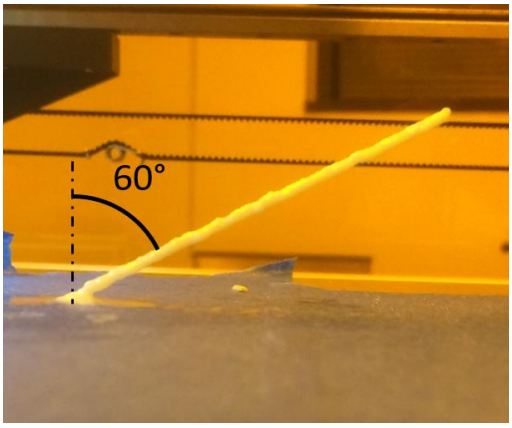


Figure 34: Results of the test printing of a single 60˚ overhanging structure

Figure 35 is a snapshot during printing with a toolpath having a gradual overhanging angle transition, which produced nearly a 90˚ overhanging angle. Figure 36 shows various single-pass overhanging structures ranging from 15˚ up to 60˚ with RGD 525. The quality of printing overhanging structure is repeatable at 60˚.

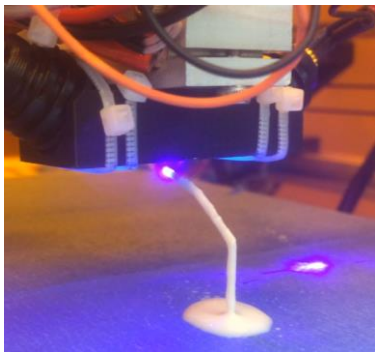

Figure 35: A snapshot of the printing process

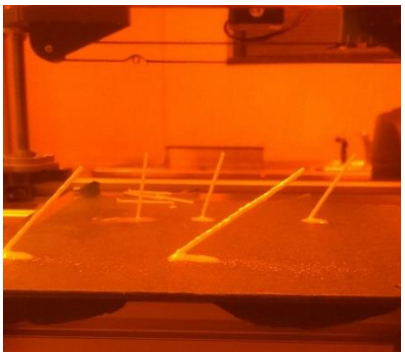

Figure 36: demonstration of repeatable printing quality of overhanging

Some issues were observed during the experiment. As the angle of overhanging approached to the limit where the material jet became perpendicular to the structure (*i.e.*, overhanging angle of 90 degrees), material waste (uncured residue) began to increase and the surface unevenness became noticeable. This physical limitation can be potentially resolved by a 5- or 6-axis motion

stage to orient the nozzle angle against the build direction. Other issues are related to inconsistent flow rate and jetting profile as well as unpredicted atomization, coalescence, or deposition. These will require further fluid characterization and mechanical design to better account for fluid properties, thus being able to attain accurate material jetting.

In addition, the proposed model will be particularly useful for when the process is discretized. For example, discretization of this process into 50 - 200 μm segments, which is the range of the mechanical resolutions of the motion stage, curing of projected resins can be ensured while it allows generating desired geometries with a sufficient printing resolution. Although developments of the algorithm generating the toolpath for the proposed printing method is necessary, the proposed process model can be applied for printings with complex geometries by the discretization of the process.

## 4.7 Conclusion

To correlate all parameters defined in the previous chapters, a process models for the designed printing process was proposed. Assuming steady material flowrate, complete curing of material, and continuous feeding in z-direction, the geometry feature size ($R$) was defined as a function of the flowrate and the printing speed. This allows the system to control its flowrate and printing speed simultaneously from the traditional machining language. Adapting Jacob's model, a curing process was modeled with the assumptions, greater laser beam radius than $R$ and half of the Gaussian irradiance for deposited resin. The curing criteria for the process was defined; the material deposited will be completely cured if the curing depth from each laser beam exceeds the predicted feature size (*i.e.*, $C_d > R$). With a constant flowrate of 0.5 $mm^3/s$, an optical power of

0.78 mW, and a beam diameter of 0.5 mm, the process was simulated by the model. The plotted results showed the ranges of the printing speed and suggested that 1 mm/s will completely cure all four photopolymers for the given parameters and material properties. With the printing speed of 1 mm/s, a series of printing test was conducted. FLX980 having stiffness of shore A 26-28, did not complete the print due to the low stiffness because it began to collapse after it reached 2-3 mm height. However, other resins having higher stiffness (shore D 75 to 88) showed noticeable support-free capabilities up to 90˚ and repeatable overhanging angle of 60˚. Some discrepancy between the predicted feature size and actual feature size was observed. The radius of printed geometry size was 0.5 to 0.6 mm, whereas the predicted radius was 0.4 mm. This may result from the uncertainty in flowrate measurement that can be seen in the uneven surface finish of the printed structures. Further fluid characterization and mechanical designs for fluid properties are needed to attain accurate material jetting.

# **5.** SUMMARY

This research summarizes the overall concept of the self-supported 3D printing and the development of this new printing method from mechanical design, material characterization, process modeling, to implementations. It was found that the photopolymerization can be characterized by the Jacob's model with identifying two dominant properties of photopolymerization, penetration depth and critical exposure, for the designed printing process. By controlling the temperature, the viscosity of photopolymers was adjusted for jetting to generate a steady state volumetric flow of 0.5 $mm^3/s$ with an actuation frequency of 15 Hz of the fabricated jetting device. For these parameters, a simple model to predict curing process was created by adapting Jacob's model that is used for conventional vat photopolymerization process. To validate the proposed model, a series of printing test was conducted with a printing speed of 1 mm/s, which ensure the curing of all photopolymers used in the study. The test demonstrated a projected UV-resin for self-supported 3D printing up to 60˚ overhanging structure consistently and up to 90˚ overhanging structure for some limited conditions. The results demonstrated its great capability for overhanging printings due to its nature of non-contacting process, which resolves the dragging issues of extrusion-based printing method.

If successful, this technology is expected to build complex geometries on any surfaces or against the direction of gravity when the system is equipped with a 5- or 6-axis motion stage. This can be particularly beneficial to internal structures or truss structures where support material would preferably not be applied. On the other hand, the results also unveiled several limitations and uncertainties associated with fluid dynamics, which require more fundamental studies. This includes characterization of surface tension, viscosity, shear effects, and temperature effects as

well as establishing a calibration method for the jetting process, preferably with a high-speed camera. For the process modeling, the modified Jacobs' model was found applicable to this new 3D printing process. Despite multiple idealized assumptions, the model provided a feasible range of printing speed to ensure the curing process. To further validate and refine the model, the jet profile, laser irradiance distribution, print cross-section, and its level of cure all need to be determined. Also, the non-linearity among printing speed, volumetric flow rate, and laser power should be considered. Lastly, this study was utilized a 3-axis motion stage instead of 5- or 6-axis as a simplification. For the further development of the proposed printing process, the motion control and its toolpath planning for the multi-degree of freedom printing process needs to be studied.

REFEERENCES


[1] Ultimaker, "Cura-support-settings," Ultimaker, 2018. [Online]. Available: https://ultimaker.com/en/resources/20422-cura-support-settings. [Accessed August 2018].

[2] P. Cain, "Supports in 3D Printing: A technology overview," 3D Hubs, 2018. [Online]. Available: https://www.3dhubs.com/knowledge-base/supports-3d-printing-technology-overview. [Accessed August 2018].

[3] P. Zelinski, "7 Helpful Numbers Quantify Design Rules for Additive Manufacturing," Additive Manufacturing, 21 November 2016. [Online]. Available: https://www.additivemanufacturing.media/blog/post/7-helpful-numbers-quantify-design-rules-for-am. [Accessed August 2018].

[4] FormLabs, "FORMLABS DESIGN GUIDE," [Online]. Available: https://formlabs.com/media/upload/formlabs-design-guide.pdf. [Accessed August 2018].

[5] M. Baumers, M. Holweg, J. Rowley,, "The economics of 3D Printing: A total cost perspective - project report," [Online]. Available: https://www.sbs.ox.ac.uk/sites/default/files/research-projects/3DP-RDM_report.pdf. [Accessed August 2018].

[6] M. Faes, E. Ferraris, D. Moens,, "Influence of Inter-layer Cooling time on the Quasi-static Properties of ABS Components Produced via Fused Deposition Modelling," vol. 42, pp. 748-753, 2016.

[7] SkyGreen, " SKYGREEN JN200 Glycol Modified Copolyester Resin - Processing Guidelines for Injection Moulding," [Online]. Available: http://www.southlandpolymers.com/pdf/petg/skygreen_JN200_processing_English.pdf. [Accessed August 2018].

[8] Farahani R, Label L, Therriault D, et al, "Processing parameters investigation for the fabrication of self-supported and freeform polymeric microstructures using ultraviolet-assisted three-dimensional printing.," *Journal of Micromechanics and Microengineering*, vol. 24, no. 5, pp. 1-12, 2014.

[9] ] Wu C, Dai C, Fang G, Liu Y, Wang C, et al., "RoboFDM: A robotic system for support-free fabrication using FDM," in *IEEE International Conference on Robotics and Automation (ICRA),* Singapore, 2017.

[10] Vanek J, Galicia JAG, Benes B, Mech R, Carr N, Stava O, et al., "PackMerger: A 3D Print Volume Optimizer," *Comput Graph Forum,* no. 33, pp. 322-32, 2014.

[11] J. Borsuk, "UV Curing in an Inerted Atmosphere – Equipment Updat," in *RadTech UV & EB Technical Conference* , Chikago, IL, 2014.

[12] J. PF, "Fundamentals of Stereolithography.," in *International Solid Freeform Fabrication Symposium*, Austin, TX, 1992.

[13] Lee JH, Prud'homme RK, Aksay IA, "Cure depth in photopolymerization: Experiments and theory," *Journal of Materials Research,* vol. 16, pp. 3536-44, 2011.

[14] Gibson I, Rosen D, Stucker B, , Additive Manufacturing Technologies, New York: Springer, 2014.

[15] T. Scherzer, U. Decker, "The effect of temperature on the kinetics of diacrylate photopolymerizations studied by Real-time FTIR spectroscopy," *Polymer,* vol. 41, no. 21, pp. 7681-90, 2000.

[16] L. Sperling, Introduction to Physical Polymer Science, New York: John Wiley and Sons, 2011.

[17] J. Bennett, "Measuring UV curing parameters of commercial photopolymers used in additive manufacturing," *Additive Manufacturing,* vol. 18, pp. 203-12, 2017.

[18] Stratasys Ltd., "PolyJet Materials Data Sheet," 2016. [Online]. Available: http://usglobalimages.stratasys.com/Main/Files/Material_Spec_Sheets/MSS_PJ_PJMaterialsDataSheet.pdf?v=635785205440671440. [Accessed August 2018].

[19] MakerJuice Labs, "Substance G+ Datasheet.," [Online]. Available: https://cdn.shopify.com/s/files/1/1224/0904/files/GPlus-TDS.pdf?5013488679945133065 .